

# Dominant orbital magnetization in the prototypical altermagnet MnTe

Chao Chen Ye,<sup>1</sup> Karma Tenzin,<sup>1</sup> Jagoda Sławińska,<sup>1,\*</sup> and Carmine Autieri<sup>2,3,†</sup>

<sup>1</sup>*Zernike Institute for Advanced Materials, University of Groningen,  
Nijenborgh 3, 9747 AG Groningen, The Netherlands*

<sup>2</sup>*International Research Centre MagTop, Institute of Physics,  
Polish Academy of Sciences, Aleja Lotników 32/46, PL-02668 Warsaw, Poland*

<sup>3</sup>*SPIN-CNR, UOS Salerno, IT-84084 Fisciano (SA), Italy*

Altermagnetism is an unconventional form of antiferromagnetism characterized by momentum-dependent spin polarization of electronic states and zero net magnetization, arising from specific crystalline symmetries. In the presence of spin-orbit coupling (SOC) and broken time-reversal symmetry, altermagnets can exhibit finite net magnetization and anomalous Hall effect (AHE), phenomena typically associated with ferromagnets. Due to the dependence of AHE on magnetization, understanding the interplay between spin and orbital contributions to magnetization is essential for interpreting experiments and designing altermagnetic devices. In this work, we use density functional theory to investigate the intrinsic spin and orbital magnetization of the magnetic ground state of the prototypical altermagnet  $\alpha$ -MnTe. We find that SOC induces weak ferromagnetism through spin canting, accompanied by a slight in-plane rotation of the Néel vector. Notably, we identify a significant net orbital magnetization of  $0.176 \mu_B$  per unit cell oriented along the  $z$ -axis, while the spin magnetization in the same direction is much smaller at  $0.002 \mu_B$ . By varying the chemical potential, we show that the spin magnetization is tunable through hole doping, whereas the orbital magnetization remains robust against carrier density changes. These results highlight the important role of orbital magnetization and establish its relevance for orbital-based phenomena in altermagnets.

## INTRODUCTION

Altermagnetism is a recently identified form of antiferromagnetism, characterized by nonrelativistic spin splitting of electronic bands in momentum space despite a vanishing net magnetization, and is predicted to emerge in a broad range of material classes [1–9]. It has attracted attention for its potential in highly efficient spin-current generation [10], optical altermagnetic switch [11], anomalous Hall effect with vanishing net magnetization [12, 13], giant tunneling magnetoresistance [14, 15], antiferromagnetic spintronics [16, 17], spin caloritronics [18] and Josephson junctions [19], among other applications. Its existence relies on the condition that the electronic charge of spin-up (down) atoms maps onto spin-down (up) ones through symmetry operations involving rotations - whether proper or improper, symmorphic or nonsymmorphic - but not by pure inversion or translation. This symmetry constraint gives rise to characteristic  $d$ -wave,  $g$ -wave, or  $i$ -wave patterns of nonrelativistic spin polarization in momentum space [3]. Such patterns are absent in antiferromagnets that preserve combined time-reversal (T) and spatial symmetries of inversion (P) or lattice translation ( $\tau$ ) [20, 21].

Materials that exhibit a small net magnetization induced by SOC are called *weak ferromagnets* [22]. SOC generates effective antisymmetric interactions between spins [23], most notably the staggered Dzyaloshinskii–Moriya interaction (DMI) [24, 25], which is closely linked to orbital effects [26]. Several recent works aim to classify the different types of SOC-driven antisymmetric interactions between the spins [21, 27–32]. In weak ferromagnets, the magnitude of the net magnetic moment is determined by the interplay among magnetic

exchange interactions, magnetocrystalline anisotropy, and SOC-induced effects. Most commonly, it appears via spin canting - a small deviation from perfect antiferromagnetic alignment. Since magnetic exchange generally dominates over SOC, the resulting canting angles are usually small, often less than  $1^\circ$  [24], unless the magnetic atoms are heavy transition metals [33].

$\alpha$ -MnTe is a prototypical altermagnet, known for exhibiting one of the largest nonrelativistic spin splittings of electronic bands [34]. It has been extensively studied both experimentally and theoretically [35–44]. The same symmetries responsible for spin splitting also generate the SOC-driven antisymmetric spin interactions [24], though their magnitudes are not directly correlated, as the former depends on kinetic parameters and the latter on the SOC strength and SOC order [27]. In MnTe, broken time-reversal symmetry and SOC lead to net spin magnetization [45] and the anomalous Hall effect (AHE) [46]. Given that AHE can arise from the orbital magnetization [47–49], the large AHE observed in MnTe may indicate a significant orbital contribution. Note that also in an isostructural material, FeS, AHE is observed at room temperature [12]. Another key factor for weak ferromagnetism is the magnetocrystalline anisotropy, which must be small to allow spin canting. In MnTe, this anisotropy was recently estimated to be  $K_2 = 40 \mu\text{eV}$  [50], where  $K_2 S_z^2$  is the energy cost of spins acquiring a  $z$ -component. Overall, understanding orbital magnetization is crucial for advancing studies on weak ferromagnetism and related orbital-driven phenomena in altermagnets [51, 52].

In this work, we perform *ab initio* simulations to quantitatively investigate spin and orbital magnetization in the altermagnetic MnTe. Our goal is to identify the origin

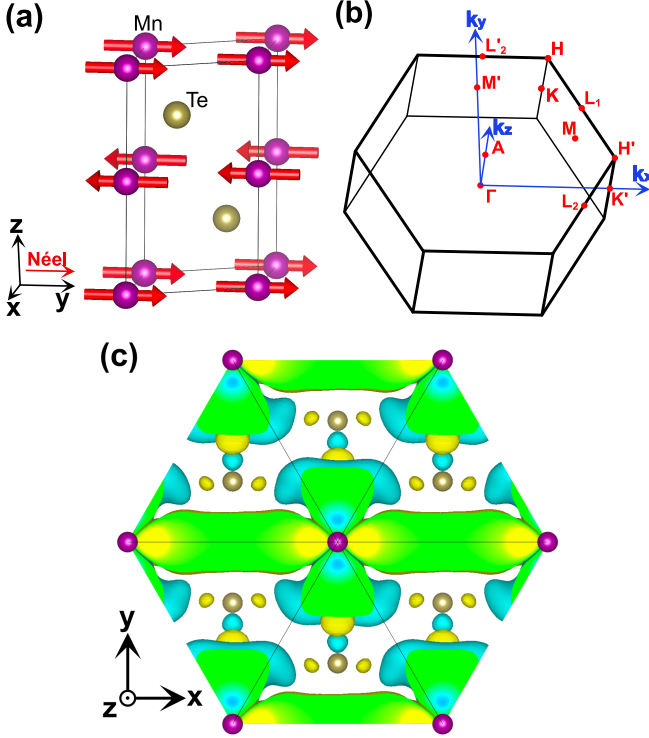


Figure 1. **Structure and charge density of MnTe.** (a) Crystal structure with the magnetic moment orientation along the  $y$ -axis. (b) The corresponding hexagonal Brillouin zone. (c) Difference between the charge densities of the Néel vector along the  $y$ -axis and  $x$ -axis for the isosurface  $1.5 \cdot 10^{-6} e/\text{\AA}^3$ . The blue and yellow colors indicate the positive and negative values of the charge differences, respectively. The breaking of  $\{6_{001}^\pm|0, 0, \frac{1}{2}\}$  and  $\{3_{001}^\pm|0\}$  symmetries is observed, while the inversion  $\{\bar{1}|0\}$  and  $\{2_{001}|0, 0, \frac{1}{2}\}$  symmetries are preserved.

of these two contributions, their magnitudes with respect to doping, and to unveil the importance of orbital magnetization. We start by exploring the symmetries present in this hexagonal system through the analysis of charge density differences and relativistic spin-resolved electronic structures. This analysis, combined with the calculation of spin and orbital magnetization for different doping levels, reveals that they are both present in the insulating phase. Lastly, we show that orbital magnetization is aligned primarily along the  $z$ -direction, with the net orbital contribution two orders of magnitude stronger than the spin counterpart. While the net spin magnetization can be tuned by hole carriers, the orbital magnetization remains nearly constant over a large energy range.

## STRUCTURAL AND ELECTRONIC PROPERTIES

### Symmetries of the system

In this subsection, we introduce the notation for the crystal structure and we report the electronic properties.

$\alpha$ -MnTe is an intrinsic  $p$ -type doped magnetic semiconductor with a Néel temperature of around 310 K [53–56] and a large band gap [56, 57]. The term  $\alpha$  refers to the hexagonal nickeline crystal structure, built by alternating layers of Mn and Te atoms, described by the  $P6_3/mmc$  (#194) space group, which only considers the symmetries relating atomic positions in the crystallographic lattice. Introducing magnetic moments onto the Mn atoms, assuming the Néel vector along the  $y$ -axis, imposes additional symmetry restrictions which lower the symmetry to the magnetic space group  $Cm'c'm$  (#63.462) [58]. This configuration is depicted in Fig. 1(a). In terms of the Seitz notation, where the prime symbol indicates the preservation of the time-reversal operation, we identified eight symmetries in Cartesian coordinates that are preserved even in the presence of SOC-induced magnetic canting. These are:  $\{1|0\}$ ,  $\{\bar{1}|0\}$ ,  $\{2_{001}|0, 0, \frac{1}{2}\}$ ,  $\{m_{001}|0, 0, \frac{1}{2}\}$ ,  $\{2'_{010}|0, 0, \frac{1}{2}\}$ ,  $\{m'_{010}|0, 0, \frac{1}{2}\}$ ,  $\{2'_{100}|0\}$  and  $\{m'_{100}|0\}$ , as determined using `Spglib` [59, 60].

The corresponding Brillouin zone and all relevant high-symmetry points are shown in Fig. 1(b). In the collinear magnetization case, we named the  $k$ -points with opposite spin-momentum locking with different indexes as  $L_1$  and  $L_2$ ; this  $60^\circ$  alternating pattern is linked to a threefold rotational symmetry, and the absence of the sixfold rotation symmetry. However, we should note that the Néel vector along the  $y$ -axis reduces it to  $\{2_{001}|0, 0, \frac{1}{2}\}$  symmetry, which breaks the alternating pattern. Therefore, we named  $L'_2$  the two  $k$ -points along the  $k_y$  direction, and we leave  $L_1$  and  $L_2$  for the other four  $k$ -points as illustrated in Fig. 1(b). The breaking of the  $\{6_{001}^\pm|0, 0, \frac{1}{2}\}$  symmetry is also evident in the real space, where the charge density difference between Néel vectors along the  $y$ - and  $x$ -axes retains only  $\{2_{001}|0, 0, \frac{1}{2}\}$  symmetry, confirming broken  $\{3_{001}^\pm|0\}$  symmetry [36, 38]. The calculated real-space charge difference is presented in Fig. 1(c).

### Spin density of states

We start with calculating the site-projected, energy-resolved magnetization density, denoted as  $\mathbf{S}^{\text{Mn}_1}$  and  $\mathbf{S}^{\text{Mn}_2}$  for the projections onto  $\text{Mn}_1$  and  $\text{Mn}_2$ , respectively. We refer to these quantities hereafter as the spin density of states. The Néel vector is defined as  $\mathbf{N} = \mathbf{S}^{\text{Mn}_1} - \mathbf{S}^{\text{Mn}_2}$ , while the spin magnetization per unit cell is given by  $\mathbf{M}^{\text{spin}} = \mathbf{S}^{\text{Mn}_1} + \mathbf{S}^{\text{Mn}_2}$ . The calculated spin density of states is reported in Fig. 2. Note that only the spin angular momentum is considered; the orbital contribution to the magnetization will be addressed in the next section.

The dominating spin component,  $S_y$ , shown in Fig. 2(b), is orders of magnitude larger than the others and gives the main contribution to the total density of states (DOS). The spin components  $S_y$  of  $\text{Mn}_1$  and  $\text{Mn}_2$  are equal and opposite. In addition, we plot the total DOS, including all atoms, in green; we can observe that the relativistic

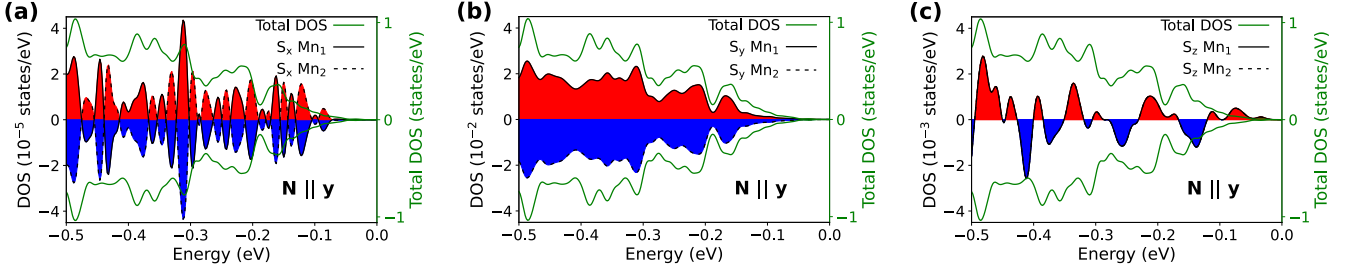


Figure 2. **Relativistic spin density of states in the valence bands for MnTe with Néel vector along the  $y$ -axis ( $N \parallel y$ ).** (a)  $S_x$  is the component responsible for the slight rotation of the Néel vector in the  $xy$ -plane. (b)  $S_y$  is the main component of the Néel vector. (c)  $S_z$  component is responsible for the weak ferromagnetism along the  $z$ -axis. Positive and negative spin contributions are shown in red and blue, respectively. The total DOS is overlaid in green in all panels.

spin density of states of the  $S_y$  component resembles the total DOS. The spin components  $S_x$  of the  $Mn_1$  and  $Mn_2$  are also equal and opposite, as shown in Fig. 2(a). Based on the calculated relativistic spin density of states, we can see that there is a slight in-plane rotation of the Néel vector. The rotation of the Néel vector is not included in the lowest-order term  $M_z N_y (3N_x^2 - N_y^2)$  [27], implying that it arises from a higher-order SOC-driven interaction. This rotation of the Néel vector depends on the energy and, therefore, can be manipulated by doping.

The  $S_z$  component of spin density of states is equal and has the same sign for both  $Mn_1$  and  $Mn_2$ , as can be seen by the overlap of solid and dashed lines in Fig. 2(c); this component generates the weak ferromagnetism. We can also observe that the spin density of  $S_z$  oscillates as a function of the energy. This oscillation is related to the fact that the weak ferromagnetism is proportional to the SOC-driven antisymmetric interaction. The SOC-driven parameter (named  $D_2$  in the Supplementary Material) oscillates as a function of the energy as the DMI [61].

To summarize, we have the following relations for the integrated spin components  $S_x^{Mn_1} = -S_x^{Mn_2}$ ,  $S_y^{Mn_1} = -S_y^{Mn_2}$ ,  $S_z^{Mn_1} = S_z^{Mn_2}$  with the order relation being  $S_y^{Mn_1} \gg S_z^{Mn_1} \gg S_x^{Mn_1}$ . Although the value of  $S_x^{Mn_1}$  is extremely small to give sizable effects, it is interesting to note that it is not zero by symmetry. Since the integrals of  $S_x$  and  $S_y$  are zero by symmetry for every value of the Fermi level, in the rest of the paper, we will focus on the  $S_z$  component projected on the band structure.

### Altermagnetic electronic structure with SOC

Relativistic altermagnetic band structures calculated along different high-symmetry lines are presented in Fig. 3. These calculations reveal signatures of both magnetic ordering, associated with the local magnetization around Mn atoms, and strong SOC originating from Te atoms [38, 44, 56, 62]. Although Fig. 3(a) indicates an indirect band gap of 0.68 eV between the A and K points, smaller than the experimental value of approximately 1.27 eV [56], we

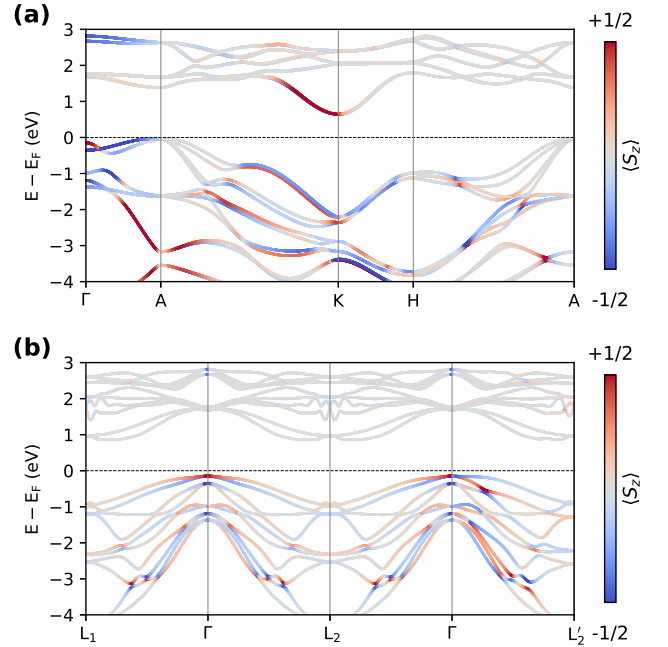


Figure 3. **Relativistic band structure with the  $S_z$  component of the spin texture indicated by the color scale on the side.** We plot the band structure along the  $k$ -path (a)  $\Gamma - A - K - H - A$  and (b)  $L_1 - \Gamma - L_2 - \Gamma - L_2$ . The Fermi energy is set at the VBM.

note that this discrepancy will not affect our conclusions, as MnTe is intrinsically  $p$ -type doped and our analysis is focused on the valence band region. Additionally, we anticipate that the valence band minimum (VBM) is not at the high-symmetry point A, instead, it is located along the  $\Gamma - K'$  line (see the next section and Fig. 5).

In terms of the orbital character of the electronic states, it is well established that the orbitals near the valence band maximum and conduction band minimum (CBM) in MnTe are mainly composed of "Te-5 $p$  + Mn-3 $d$ " and "Mn-3 $d$  + Mn-4 $s$ " states, respectively [56, 62–64]. The bands at the high-symmetry points  $\Gamma$  and A are fourfold degenerate. More specifically, the top of the valence band

at the A point is doubly degenerate, dominated by Te  $p_x$ - $p_y$  orbital character, while the singly degenerate  $p_z$ -like state lies farther below the Fermi level. We note that the nonrelativistic band structure hosts the largest spin splitting along the  $\Gamma - L$  directions, which does not strictly hold anymore in the relativistic case.

The coloring of the bands in Fig 3 represents the  $S_z$  component of the spin texture and clearly indicates its strong presence across the entire band structure when the Néel vector is oriented along the  $y$ -axis [34]. Focusing on the  $L_1 - \Gamma - L_2$   $k$ -path, we find that the projection of the main  $S_y$  component is opposite along the two paths, as detailed in the Supplementary Material. In contrast, the  $S_z$  component - responsible for weak ferromagnetism - remains the same along both  $L_1 - \Gamma$  and  $\Gamma - L_2$  in Fig. 3(b). Notably, our band structure is asymmetric between  $L_2$  and  $L'_2$ , confirming the sixfold symmetry breaking [34].

Finally, we examine the Fermi pockets across the BZ resulting from a small hole doping, as shown in Fig. 4. These pockets correspond to the isosurface  $E - E_F \approx -0.10$  eV, located below VBM. The spin texture components  $S_x$  and  $S_y$  are shown in Fig. 4(a) and (b), respectively. The most pronounced feature, at first sight, is the  $g$ -wave spin polarization pattern, visible in the larger pockets near the BZ edges, where the spin direction changes every  $60^\circ$ , reminiscent of the nonrelativistic case. This pattern is absent in Fig. 4 (c), which shows the  $S_z$  component. While

the alternating  $g$ -wave structure is clearly observed for the in-plane components  $S_x$  and  $S_y$ , no higher rotational symmetry beyond a twofold rotation can be inferred from the dominant red lobes in the  $S_z$  texture. The Fermi pockets illustrated in Fig. 4(d) exhibit significantly larger sizes for  $+S_z$  compared to  $-S_z$ , aligning with the symmetry effects of the material. However, this size difference is hard to observe experimentally [34]. Additionally, we highlight the  $S_z$  contributions along the  $k_z$ -direction, displayed inside the white color Fermi pockets in Fig. 4(c).

### Spin and orbital magnetization

We now numerically estimate the total magnetization per unit cell,  $\mathbf{M} = \mathbf{M}^{spin} + \mathbf{M}^{orb}$ , consisting of both spin and orbital contributions. We only consider intrinsic mechanisms responsible for the magnetization; the extrinsic mechanisms, such as structural and magnetic defects, will not be considered in the present paper [65]. In particular, the orbital magnetization is expected to be relevant for materials with large SOC and it is present in systems with large DMI [24, 26, 38, 66]; however, few results have been reported for altermagnets. The calculations of spin and orbital magnetization are evaluated as the sum of contributions from all Bloch states over the entire Brillouin zone [67–73], using the following equations:

$$\begin{aligned} \mathbf{M}^{spin} &= \sum_n \int_{BZ} \frac{d\mathbf{k}}{(2\pi)^3} f_n(\mathbf{k}) \mathbf{M}_n^{spin}(\mathbf{k}) = \frac{g_s \mu_B}{(2\pi)^3} \sum_n \int_{BZ} d\mathbf{k} f_n(\mathbf{k}) \langle \psi_{n\mathbf{k}} | \hat{\mathbf{S}} | \psi_{n\mathbf{k}} \rangle, \\ \mathbf{M}^{orb} &= \sum_n \int_{BZ} \frac{d\mathbf{k}}{(2\pi)^3} f_n(\mathbf{k}) \mathbf{M}_n^{orb}(\mathbf{k}) = \frac{e}{2\hbar(2\pi)^3} \text{Im} \sum_n \int_{BZ} d\mathbf{k} f_n(\mathbf{k}) \left\langle \frac{\partial u_{n\mathbf{k}}}{\partial \mathbf{k}} \right| \times \left( \hat{H}_{\mathbf{k}} + E_{n\mathbf{k}} - 2E_F \right) \left| \frac{\partial u_{n\mathbf{k}}}{\partial \mathbf{k}} \right\rangle, \end{aligned} \quad (1)$$

where  $g_s$  is the spin  $g$ -factor,  $\mu_B$  is the Bohr magneton,  $e$  is the elementary charge, and  $f_n(\mathbf{k})$  is an electronic distribution function. The operator  $\hat{\mathbf{S}}$  represents the spin,  $\hat{H}_{\mathbf{k}}$  is the Bloch Hamiltonian, and  $|\psi_{n\mathbf{k}}\rangle = e^{i\mathbf{k}\cdot\mathbf{r}} |u_{n\mathbf{k}}\rangle$  are Bloch eigenstates with eigenvalues  $E_{n\mathbf{k}}$ . The spin expectation values have already been discussed in the previous sections; now, we focus on orbital magnetization calculated along different paths in BZ.

Figure 5 shows the  $k$ -resolved orbital magnetization evaluated with the chemical potential shifted to simulate sizable hole doping. For reference, the upper panel displays the corresponding band structure near the selected chemical potential to facilitate the interpretation of the orbital magnetization behavior along various  $k$ -paths. We observe that the most prominent orbital magnetization peak in the valence band appears along the  $\Gamma - A$  path, i.e., along the  $k_z$ -axis. The  $M_x^{orb}(\mathbf{k})$  and  $M_y^{orb}(\mathbf{k})$  components fluctuate around zero and are at least an order of magnitude smaller than the dominant  $M_z^{orb}(\mathbf{k})$

component (see Supplementary Materials).

To emphasize the importance of orbital magnetization in MnTe, we note that the bcc Fe exhibits peaks that are at least one order of magnitude smaller [71] than the peaks displayed in Fig. 5. Additionally, we identify inverted peaks at  $L_1$  and  $L'_2$  which originate from bands located deeply in the occupied part of the spectrum - this is a consequence of the cumulative nature of the orbital magnetization. The above information also discloses that the origin of magnetic canting due to SOC comes from the holes in the valence band, specifically the Mn-3d orbitals.

Finally, we evaluate the net spin and orbital magnetization as a function of the chemical potential, governed by Eq. (1), which relates total magnetization to the Fermi level. The results for the spin magnetization are shown in Fig. 6(a). Due to the symmetry of the SOC-driven antisymmetric interaction, the net spin magnetization has vanishing components in the  $x$ - and  $y$ -directions, i.e.,  $M_x^{spin} = M_y^{spin} = 0$ . In contrast, the  $z$ -component re-



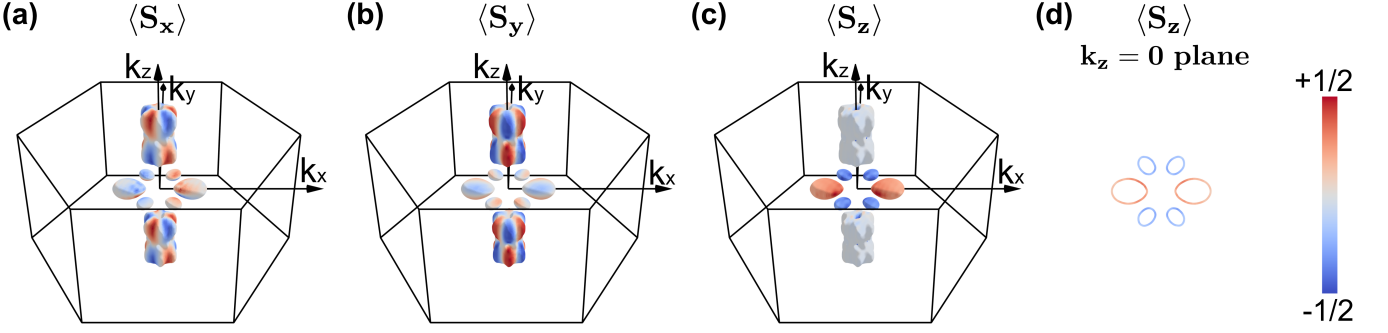


Figure 4. **Spin-projected isosurfaces with the Fermi level in the valence band.** Isosurface  $E - E_F \approx -0.10$  eV colored by the component of the spin texture (a)  $S_x$ , (b)  $S_y$  and (c)  $S_z$ . (d) The isoenergy contours for the  $k_z = 0$  plane together with the spin texture component  $S_z$  is highlighted.

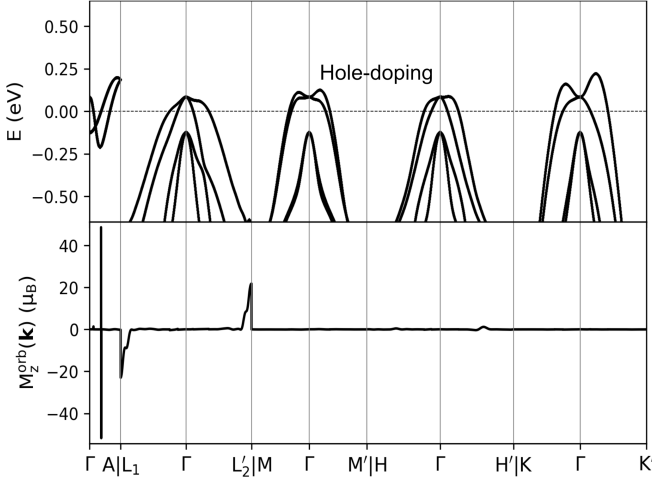


Figure 5. **Calculated k-resolved orbital magnetization  $M_z^{\text{orb}}(\mathbf{k})$  for the Fermi level in the valence band.** Orbital magnetization  $M_z^{\text{orb}}(\mathbf{k})$  along  $k$ -paths for  $E_F = E_{VBM} - 0.23$  eV (Fermi level in the valence band). Importantly, the  $x$ - and  $y$ -components are at least one order of magnitude smaller than the  $M_z^{\text{orb}}(\mathbf{k})$  as shown in the Supplementary Material. Their contributions come from bands located deeply in the occupied part due to the cumulative aspect of orbital magnetization.

mains finite across all values of the chemical potential and does not vanish even within the band gap. This implies that altermagnets can exhibit weak ferromagnetism even in the absence of doping. However, this effect is strongly suppressed by the presence of a large band gap.

Weak ferromagnetism arises from the spin-nonconserving nature of spin-orbit coupling (SOC), which enables mixing between spin-up and spin-down states on the same atomic site. When there is a large energy gap between the spin-up and spin-down manifolds relative to the SOC strength, this mixing becomes negligible (see Supplementary Material), resulting in an almost vanishing imbalance between spin-up and spin-down components on each site. As a consequence, weak ferromagnetism is expected to be suppressed in

wide-gap, high-spin, undoped systems. This suppression is confirmed numerically: at the Fermi level, where the valence band is fully occupied, the net spin magnetization reaches a near-minimum in MnTe. Our DFT calculations yield a total spin magnetization of approximately  $0.002 \mu_B$  per unit cell. Each Mn atom contributes about  $0.001 \mu_B$  along the  $z$ -axis, compared to a total spin moment of  $4 \mu_B$ , from which we obtain that the canting angle (described in Supplementary Material) is  $\bar{\theta} = 0.01^\circ$ .

The components of the net orbital magnetization calculated as a function of the chemical potential are reported in Fig. 6(b). Similarly to spin magnetization, the orbital magnetization is constant inside the band gap due to the absence of electronic states. In this case, however,  $M_x^{\text{orb}} \simeq 0$  is not exactly zero but on the order of  $10^{-5} \mu_B$ . Similarly,  $M_y^{\text{orb}} \simeq 0$  but its magnitude is around  $10^{-4} \mu_B$ . The dominant term is  $M_z^{\text{orb}}$ , reaching approximately  $-0.176 \mu_B$  per unit cell within the band gap. Notably, the orbital and spin magnetization have the same direction, but the orbital contribution is two orders of magnitude larger. This indicates the crucial role of orbital magnetization in MnTe, whose magnitude exceeds that of bcc Fe, despite MnTe having a total magnetization an order of magnitude smaller [71, 74–76]. Notably, this finding is consistent with prior theoretical studies, which also reported orbital magnetization dominating over spin contributions in weak ferromagnets [31].

Experimentally, the net magnetization - including both spin and orbital parts - is in the range of  $10^{-4}$  to  $10^{-3} \mu_B$  per Mn atom [45, 77], significantly lower than our theoretical prediction  $M_z^{\text{tot}} = M_z^{\text{spin}} + M_z^{\text{orb}} \approx -0.002 + (-0.176) = -0.178 \mu_B$ . This discrepancy can be attributed to the presence of altermagnetic domains, which tend to compensate each other, leading to a reduced observed net magnetization [78, 79].

In summary, along the  $z$ -axis, the orbital contribution clearly dominates, confirming its central role for shaping weak ferromagnetism. These results indicate the need to incorporate orbital contributions, via Eq. (1), for a complete and accurate description of altermagnetic materials.

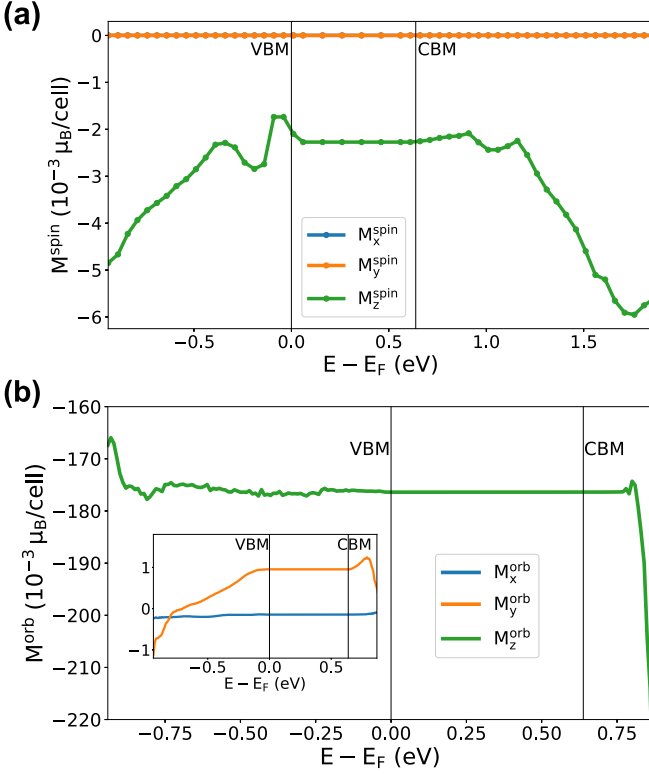


Figure 6. **Net spin and orbital magnetizations of MnTe in the low-energy window.** (a) Spin magnetization components, the  $M_x^{spin}$  and  $M_y^{spin}$  components are exactly zero as expected by symmetry. (b) Orbital magnetization component.  $M_z^{orb}$  is the dominant contribution, while  $M_x^{orb}$  and  $M_y^{orb}$  are shown in the inset. The  $y$ -axis of the inset figure displays a different range compared to the main figure. The two vertical lines indicate the VBM and CBM.

## CONCLUSIONS

In conclusion, we have performed *ab initio* density functional theory calculations for altermagnet  $\alpha$ -MnTe to investigate its spin and orbital magnetization. We have demonstrated the breaking of sixfold and threefold rotational symmetries of MnTe due to the orientation of the Néel vector, while retaining the  $\{2_{001}|0, 0, \frac{1}{2}\}$  symmetry.

We find that both spin and orbital magnetization vectors are aligned along the  $z$ -axis, perpendicular to the Néel vector direction. While spin canting leads to weak ferromagnetism, the resulting spin magnetization is small - approximately  $0.002 \mu_B$  per unit cell. The net spin magnetization is suppressed in MnTe by multiple factors: the higher-order SOC term, the wide band gap, and the large magnetic exchange. In contrast, the intrinsic orbital magnetization is substantial, reaching  $0.176 \mu_B$  per unit cell, and represents the dominant contribution to the net magnetization. Our calculated magnetization per unit cell is larger than the experimental value; this calls for a careful examination of altermagnetic domains and extrinsic magnetization contributions [65].

Finally, our results show that a finite magnetization persists in the insulating phase of  $\alpha$ -MnTe, although it is suppressed near the band gap, while hole doping enables tuning of the spin magnetization. In contrast, the orbital magnetization remains nearly constant over a wide energy range - up to 0.75 eV below the valence band maximum - demonstrating its robustness against carrier doping.

These results show the importance of orbital magnetization in altermagnets and suggests that concepts explored in spin-based altermagnetic systems may be extended to orbital phenomena. This opens new opportunities for both spin- and orbitronics as well as designing orbitronic functionalities in altermagnetic materials.

## COMPUTATIONAL DETAILS

We performed DFT calculations using Vienna *Ab initio* Simulation Package (VASP) [80–82]. The kinetic energy cutoff for the plane wave basis was set to 350 eV and the generalized gradient approximation of Perdew, Burke, and Ernzerhof was used for the exchange-correlation functional [83]. The Hubbard  $U$  for the Mn-3d orbitals was added [84], with the Coulomb repulsion  $U = 4$  eV and the Hund coupling  $J_H = 0.97$  eV [58, 85]. The energy convergence threshold was set to  $2 \cdot 10^{-5}$  eV. The structure was modeled by a hexagonal unit cell with lattice parameters equal to  $a = b = 4.134$  Å and  $c = 6.652$  Å [58]. The Brillouin zone was sampled using a mesh of  $20 \times 20 \times 12$   $k$ -points centered at  $\Gamma$ . For the spin density of states, we used a  $28 \times 28 \times 20$   $k$ -points grid. The spin-orbit coupling was taken into account in all the calculations and the symmetries were switched on. As a postprocessing step, we used Wannier90 [86] to calculate spin-polarized band structures, orbital magnetization along high-symmetry lines in the Brillouin zone, as well as the net spin and orbital magnetization as a function of chemical potential. We also employed the post-processing code PAOFLOW [87, 88] to evaluate spin-polarized Fermi pockets at different values of hole doping.

## DATA AVAILABILITY

The data that support the findings of this study will be openly available at DataVerseNL XXX after the paper is accepted.

## ACKNOWLEDGMENTS

The authors thank T. Dietl, M. Mostovoy, M. Sawicki, K. Výborný, J. Železný, V. V. Volobuev, A. Kazakov and B.J.M. van Dijk for useful discussions. We acknowledge the research program “Materials for the Quantum Age” (QuMat) for financial support. This program (registration

number 024.005.006) is part of the Gravitation program financed by the Dutch Ministry of Education, Culture and Science (OCW). C. A. was supported by the Foundation for Polish Science project “MagTop” no. FENG.02.01-IP.05-0028/23, co-financed by the European Union from the funds of Priority 2 of the European Funds for a Smart Economy Program 2021–2027 (FENG). C.A. acknowledges support from PNR MUR project PE0000023-NQSTI. J.S. acknowledges the Rosalind Franklin Fellowship from the University of Groningen. The calculations were carried out on the Dutch national e-infrastructure with the support of SURF Cooperative (EINF-10658).

## AUTHOR CONTRIBUTIONS

C.C.Y. performed all calculations and wrote the initial draft of the manuscript. K.T. performed PAOFLOW calculations. All the authors analyzed the data and participated in the discussions. J.S. and C.A. supervised the project.

---

\* [jagoda.slawska@rug.nl](mailto:jagoda.slawska@rug.nl)

† [autieri@magtop.ifpan.edu.pl](mailto:autieri@magtop.ifpan.edu.pl)

- [1] Hayami, S., Yanagi, Y. & Kusunose, H. Momentum-dependent spin splitting by collinear antiferromagnetic ordering. *J. Phys. Soc. Jpn.* **88**, 123702 (2019).
- [2] Yuan, L.-D., Zhang, X., Acosta, C. M. & Zunger, A. Uncovering spin-orbit coupling-independent hidden spin polarization of energy bands in antiferromagnets. *Nat. Commun.* **14**, 5301 (2023).
- [3] Šmejkal, L., Sinova, J. & Jungwirth, T. Beyond conventional ferromagnetism and antiferromagnetism: A phase with nonrelativistic spin and crystal rotation symmetry. *Phys. Rev. X* **12**, 031042 (2022).
- [4] Šmejkal, L., Sinova, J. & Jungwirth, T. Emerging research landscape of altermagnetism. *Phys. Rev. X* **12**, 040501 (2022).
- [5] Guo, Y. *et al.* Spin-split collinear antiferromagnets: A large-scale ab-initio study. *Mater. Today Phys.* **32**, 100991 (2023).
- [6] Tamang, R., Gurung, S., Rai, D. P., Brahimi, S. & Lounis, S. Newly discovered magnetic phase: A brief review on altermagnets (2024). 2412.05377.
- [7] Cuono, G., Sattigeri, R. M., Autieri, C. & Dietl, T. Ab initio overestimation of the topological region in Eu-based compounds. *Phys. Rev. B* **108**, 075150 (2023).
- [8] Sheoran, S. & Bhattacharya, S. Nonrelativistic spin splittings and altermagnetism in twisted bilayers of centrosymmetric antiferromagnets. *Phys. Rev. Mater.* **8**, L051401 (2024).
- [9] Fakhredine, A., Sattigeri, R. M., Cuono, G. & Autieri, C. Interplay between altermagnetism and nonsymmorphic symmetries generating large anomalous Hall conductivity by semi-Dirac points induced anticrossings. *Phys. Rev. B* **108**, 115138 (2023).
- [10] González-Hernández, R. *et al.* Efficient electrical spin splitter based on nonrelativistic collinear antiferromagnetism. *Phys. Rev. Lett.* **126**, 127701 (2021).
- [11] Vita, A. D. *et al.* Optical switching in a layered altermagnet (2025). 2502.20010.
- [12] Takagi, R. *et al.* Spontaneous Hall effect induced by collinear antiferromagnetic order at room temperature. *Nat. Mater.* **24**, 63–68 (2025).
- [13] Sheoran, S. & Dev, P. Spontaneous anomalous Hall effect in two-dimensional altermagnets. *Phys. Rev. B* **111**, 184407 (2025).
- [14] Šmejkal, L., Hellenes, A. B., González-Hernández, R., Sinova, J. & Jungwirth, T. Giant and tunneling magnetoresistance in unconventional collinear antiferromagnets with nonrelativistic spin-momentum coupling. *Phys. Rev. X* **12**, 011028 (2022).
- [15] Sun, W., Wang, M., Sa, B., Dong, S. & Autieri, C. Altermagnetizing the FeSe-like two-dimensional materials and approaching to giant tunneling magnetoresistance with Janus Cr<sub>4</sub>BN(B<sub>2</sub>) MBene electrode (2025). 2502.03165.
- [16] Shao, D.-F., Zhang, S.-H., Li, M., Eom, C.-B. & Tsymbal, E. Y. Spin-neutral currents for spintronics. *Nat. Commun.* **12**, 7061 (2021).
- [17] Shao, D.-F. *et al.* Néel spin currents in antiferromagnets. *Phys. Rev. Lett.* **130**, 216702 (2023).
- [18] Zhou, X. *et al.* Crystal thermal transport in altermagnetic RuO<sub>2</sub>. *Phys. Rev. Lett.* **132**, 056701 (2024).
- [19] Ouassou, J. A., Brataas, A. & Linder, J. dc Josephson effect in altermagnets. *Phys. Rev. Lett.* **131**, 076003 (2023).
- [20] Xiao, R.-C., Shao, D.-F., Li, Y.-H. & Jiang, H. Spin photogalvanic effect in two-dimensional collinear antiferromagnets. *npj Quantum Mater.* **6**, 35 (2021).
- [21] Cheong, S.-W. & Huang, F.-T. Altermagnetism with non-collinear spins. *npj Quantum Mater.* **9**, 13 (2024).
- [22] Dzyaloshinsky, I. A thermodynamic theory of “weak” ferromagnetism of antiferromagnetics. *J. Phys. Chem. Solids* **4**, 241–255 (1958).
- [23] Mazurenko, V. V. & Anisimov, V. I. Weak ferromagnetism in antiferromagnets:  $\alpha$ -Fe<sub>2</sub>O<sub>3</sub> and La<sub>2</sub>CuO<sub>4</sub>. *Phys. Rev. B* **71**, 184434 (2005).
- [24] Autieri, C., Sattigeri, R. M., Cuono, G. & Fakhredine, A. Staggered Dzyaloshinskii-Moriya interaction inducing weak ferromagnetism in centrosymmetric altermagnets and weak ferrimagnetism in noncentrosymmetric altermagnets. *Phys. Rev. B* **111**, 054442 (2025).
- [25] Ye, X., Cui, Q., Lin, W. & Yu, T. Spin quenching and transport by hidden Dzyaloshinskii-Moriya interactions. *Phys. Rev. B* **111**, 064401 (2025).
- [26] Moriya, T. Anisotropic superexchange interaction and weak ferromagnetism. *Phys. Rev.* **120**, 91–98 (1960).
- [27] Roig, M. *et al.* Quasi-symmetry constrained spin ferromagnetism in altermagnets (2024). 2412.09338.
- [28] Cheong, S.-W. & Huang, F.-T. Altermagnetism classification. *npj Quantum Materials* **10**, 38 (2025).
- [29] McClarty, P. A. & Rau, J. G. Landau theory of altermagnetism. *Phys. Rev. Lett.* **132**, 176702 (2024).
- [30] Schiff, H., McClarty, P., Rau, J. G. & Romhányi, J. Collinear altermagnets and their Landau theories (2024). 2412.18025.
- [31] Jo, D. *et al.* Weak ferromagnetism in altermagnets from alternating  $g$ -tensor anisotropy (2024). 2410.17386.
- [32] Solovyev, I. V., Nikolaev, S. A. & Tanaka, A. Altermagnetism and weak ferromagnetism (2025). 2503.23735.

- [33] Milivojević, M., Orozović, M., Picozzi, S., Gmitra, M. & Staviří, S. Interplay of altermagnetism and weak ferromagnetism in two-dimensional RuF<sub>4</sub>. *2D Materials* **11**, 035025 (2024).
- [34] Krempaský, J. *et al.* Altermagnetic lifting of Kramers spin degeneracy. *Nature* **626**, 517–522 (2024).
- [35] Kriegner, D. *et al.* Multiple-stable anisotropic magnetoresistance memory in antiferromagnetic MnTe. *Nat. Commun.* **7**, 11623 (2016).
- [36] Yin, G. *et al.* Planar Hall effect in antiferromagnetic MnTe thin films. *Phys. Rev. Lett.* **122**, 106602 (2019).
- [37] Mori, S., Hatayama, S., Shuang, Y., Ando, D. & Sutou, Y. Reversible displacive transformation in MnTe polymorphic semiconductor. *Nat. Commun.* **11**, 85 (2020).
- [38] Mazin, I. I. & Belashchenko, K. D. Origin of the gossamer ferromagnetism in MnTe. *Phys. Rev. B* **110**, 214436 (2024).
- [39] Devaraj, N., Bose, A. & Narayan, A. Interplay of altermagnetism and pressure in hexagonal and orthorhombic MnTe. *Phys. Rev. Mater.* **8**, 104407 (2024).
- [40] Gonzalez Betancourt, R. D. *et al.* Anisotropic magnetoresistance in altermagnetic MnTe. *npj Spintronics* **2**, 45 (2024).
- [41] Lee, S. *et al.* Broken Kramers degeneracy in altermagnetic MnTe. *Phys. Rev. Lett.* **132**, 036702 (2024).
- [42] Liu, Z., Ozeki, M., Asai, S., Itoh, S. & Masuda, T. Chiral split magnon in altermagnetic MnTe. *Phys. Rev. Lett.* **133**, 156702 (2024).
- [43] Belashchenko, K. D. Giant strain-induced spin splitting effect in MnTe, a *g*-wave altermagnetic semiconductor. *Phys. Rev. Lett.* **134**, 086701 (2025).
- [44] Takahashi, K., Huang, H.-F., Yu, J.-X. & Zang, J. Symmetry and minimal Hamiltonian of nonsymmorphic collinear antiferromagnet MnTe (2025). 2503.07951.
- [45] Kluczyk, K., Gas, K., Grzybowski, M. & *et al.* Coexistence of anomalous Hall effect and weak magnetization in a nominally collinear antiferromagnet MnTe. *Phys. Rev. B* **110**, 155201 (2024).
- [46] Gonzalez Betancourt, R. D. *et al.* Spontaneous anomalous Hall effect arising from an unconventional compensated magnetic phase in a semiconductor. *Phys. Rev. Lett.* **130**, 036702 (2023).
- [47] Śliwa, C. & Dietl, T. Orbital magnetization in dilute ferromagnetic semiconductors. *Phys. Rev. B* **90**, 045202 (2014).
- [48] Dowinton, O. & Bahramy, M. S. Orbital angular momentum driven anomalous Hall effect. *Phys. Rev. B* **105**, 235142 (2022).
- [49] Nakamura, A. *et al.* In-plane anomalous Hall effect associated with orbital magnetization: Measurements of low-carrier density films of a magnetic Weyl semimetal. *Phys. Rev. Lett.* **133**, 236602 (2024).
- [50] Dzian, J. *et al.* Antiferromagnetic resonance in  $\alpha$ -MnTe (2025). 2502.18933.
- [51] Palle, G., Ojajärvi, R., Fernandes, R. M. & Schmalian, J. Superconductivity due to fluctuating loop currents. *Sci. Adv.* **10**, eadn3662 (2024).
- [52] Sobral, J. A., Mandal, S. & Scheurer, M. S. Fractionalized altermagnets: from neighboring and altermagnetic spin-liquids to fractionalized spin-orbit coupling (2024). 2410.10949.
- [53] Uchida, E., Kondoh, H. & Fukuoka, N. Magnetic and electrical properties of manganese telluride. *J. Phys. Soc. Jpn.* **11**, 27–32 (1956).
- [54] Baniewicz, J. J., Heidelberg, R. F. & Luxem, A. H. High temperature magnetic susceptibilities of MnO, MnSe and MnTe. *J. Phys. Chem.* **65**, 615–617 (1961).
- [55] Ozawa, K., Anzai, S. & Hamaguchi, Y. Effect of pressure on the magnetic transition point of manganese telluride. *Phys. Lett.* **20**, 132–133 (1966).
- [56] Ferrer-Roca, C., Segura, A., Reig, C. & Munoz, V. Temperature and pressure dependence of the optical absorption in hexagonal MnTe. *Phys. Rev. B* **61**, 13679 (2000).
- [57] Osumi, T. *et al.* Observation of a giant band splitting in altermagnetic MnTe. *Phys. Rev. B* **109**, 115102 (2024).
- [58] Kriegner, D. *et al.* Magnetic anisotropy in antiferromagnetic hexagonal MnTe. *Phys. Rev. B* **96**, 214418 (2017).
- [59] Togo, A., Shinohara, K. & *and*, I. T. Spglib: a software library for crystal symmetry search. *STAM-M* **4**, 2384822 (2024).
- [60] Shinohara, K., Togo, A. & Tanaka, I. Algorithms for magnetic symmetry operation search and identification of magnetic space group from magnetic crystal structure. *Acta Crystallogr. A: Found. Crystallogr.* **79**, 390–398 (2023).
- [61] Hajr, A., Hariri, A., Manchon, G., Ghosh, S. & Manchon, A. Semirealistic tight-binding model for Dzyaloshinskii-Moriya interaction. *Phys. Rev. B* **102**, 224427 (2020).
- [62] Faria Junior, P. E. *et al.* Sensitivity of the MnTe valence band to the orientation of magnetic moments. *Phys. Rev. B* **107**, L100417 (2023).
- [63] Allen, J., Lucovsky, G. & Mikkelsen, J. Optical properties and electronic structure of crossroads material MnTe. *Solid State Commun.* **24**, 367–370 (1977).
- [64] Autieri, C., Śliwa, C., Islam, R., Cuono, G. & Dietl, T. Momentum-resolved spin splitting in Mn-doped trivial CdTe and topological HgTe semiconductors. *Phys. Rev. B* **103**, 115209 (2021).
- [65] Bugajewski, D., Autieri, C. & Dietl, T. Theory of bound magnetic polarons in cubic and uniaxial antiferromagnets (2025). 2505.05XXX.
- [66] Adamantopoulos, T. *et al.* Spin and orbital magnetism by light in rutile altermagnets. *npj Spintronics* **2** (2024).
- [67] Xiao, D., Shi, J. & Niu, Q. Berry phase correction to electron density of states in solids. *Phys. Rev. Lett.* **95**, 137204 (2005).
- [68] Thonhauser, T., Ceresoli, D., Vanderbilt, D. & Resta, R. Orbital magnetization in periodic insulators. *Phys. Rev. Lett.* **95**, 137205 (2005).
- [69] Ceresoli, D., Thonhauser, T., Vanderbilt, D. & Resta, R. Orbital magnetization in crystalline solids: Multi-band insulators, Chern insulators, and metals. *Phys. Rev. B* **74**, 024408 (2006).
- [70] Xiao, D., Chang, M.-C. & Niu, Q. Berry phase effects on electronic properties. *Rev. Mod. Phys.* **82**, 1959–2007 (2010).
- [71] Lopez, M. G., Vanderbilt, D., Thonhauser, T. & Souza, I. Wannier-based calculation of the orbital magnetization in crystals. *Phys. Rev. B* **85**, 014435 (2012).
- [72] Johansson, A. Theory of spin and orbital Edelstein effects. *J. Condens. Matter Phys.* **36**, 423002 (2024).
- [73] Rhonald Burgos Atencia, A. A. & Culcer, D. Orbital angular momentum of Bloch electrons: equilibrium formulation, magneto-electric phenomena, and the orbital Hall effect. *Adv. Phys.: X* **9**, 2371972 (2024).
- [74] Meyer, A. J. P. & Asch, G. Experimental  $g'$  and  $g$  values of Fe, Co, Ni, and their alloys. *J. Appl. Phys.* **32**, S330–S333



- (1961).
- [75] Hanke, J.-P. *et al.* Role of Berry phase theory for describing orbital magnetism: From magnetic heterostructures to topological orbital ferromagnets. *Phys. Rev. B* **94**, 121114 (2016).
  - [76] Kübler, J. Magnetic moments of ferromagnetic and anti-ferromagnetic bcc and fcc iron. *Phys. Lett. A* **81**, 81–83 (1981).
  - [77] Hariki, A. *et al.* X-ray magnetic circular dichroism in altermagnetic  $\alpha$ -MnTe. *Phys. Rev. Lett.* **132**, 176701 (2024).
  - [78] Amin, O. J. *et al.* Nanoscale imaging and control of altermagnetism in MnTe. *Nature* **636**, 348–353 (2024).
  - [79] Takegami, D. *et al.* Circular dichroism in resonant inelastic X-ray scattering: Probing altermagnetic domains in MnTe (2025). 2502.10809.
  - [80] Kresse, G. & Hafner, J. Ab initio molecular dynamics for liquid metals. *Phys. Rev. B* **47**, 558–561 (1993).
  - [81] Kresse, G. & Furthmüller, J. Efficient iterative schemes for ab initio total-energy calculations using a plane-wave basis set. *Phys. Rev. B* **54**, 11169–11186 (1996).
  - [82] Kresse, G. & Furthmüller, J. Efficiency of ab-initio total energy calculations for metals and semiconductors using a plane-wave basis set. *Comp. Mat. Sci.* **6**, 15–50 (1996).
  - [83] Perdew, J. P., Burke, K. & Ernzerhof, M. Generalized gradient approximation made simple. *Phys. Rev. Lett.* **77**, 3865–3868 (1996).
  - [84] Liechtenstein, A. I., Anisimov, V. I. & Zaanen, J. Density-functional theory and strong interactions: Orbital ordering in Mott-Hubbard insulators. *Phys. Rev. B* **52**, R5467–R5470 (1995).
  - [85] Antropov, V. P., Antonov, V. N., Bekenov, L. V., Kutepov, A. & Kotliar, G. Magnetic anisotropic effects and electronic correlations in MnBi ferromagnet. *Phys. Rev. B* **90**, 054404 (2014).
  - [86] Pizzi, G. *et al.* Wannier90 as a community code: new features and applications. *J. Condens. Matter Phys.* **32**, 165902 (2020).
  - [87] Buongiorno Nardelli, M. *et al.* PAOFlow: A utility to construct and operate on ab initio Hamiltonians from the projections of electronic wavefunctions on atomic orbital bases, including characterization of topological materials. *Comp. Mat. Sci.* **143**, 462–472 (2018).
  - [88] Cerasoli, F. T. *et al.* Advanced modeling of materials with PAOFlow 2.0: new features and software design. *Comp. Mat. Sci.* **200**, 110828 (2021).

## SUPPLEMENTARY MATERIAL

### RELATIVISTIC BAND STRUCTURE WITH THE IN-PLANE COMPONENTS OF THE SPIN

In this Section, we report the band structure along  $k$ -path  $L_1 - \Gamma - L_2 - \Gamma - L'_2$  for the spin components  $\langle S_x \rangle$  and  $\langle S_y \rangle$  when the Néel vector is along the  $y$ -axis. We observe in Fig. 7(b) that  $\langle S_y \rangle$  is the main components ranging from  $+\frac{1}{2}$  to  $-\frac{1}{2}$ , while  $\langle S_x \rangle$  in Fig. 7(a) vary within a much smaller range.  $L_1$  and  $L_2$  are symmetry equivalent  $k$ -points for  $\langle S_x \rangle$  in agreement with the  $z$ -component of the spin in the Fig. 3 in the main text. The  $\langle S_y \rangle$  highlights

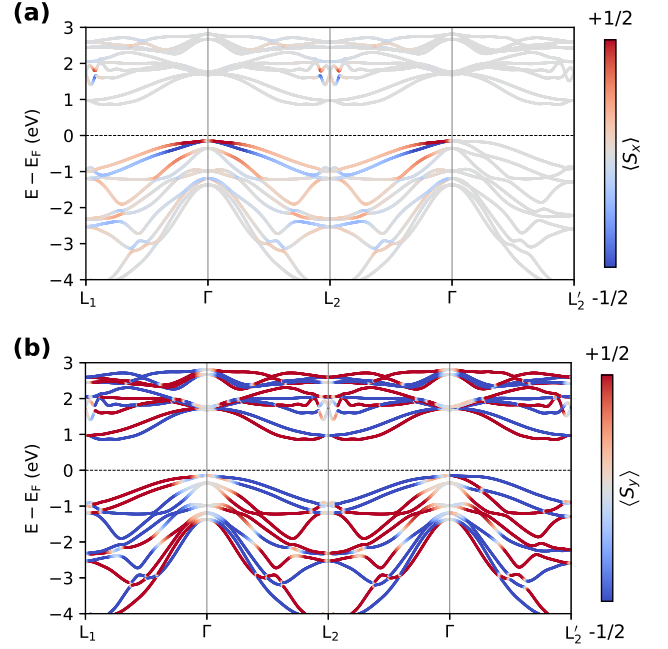


Figure 7. **In-plane components of spin texture projected on the band structure.** Band dispersion with the projection of the component (a)  $S_x$  and (b)  $S_y$ . Their magnitudes are indicated by the color scale on the side. The Néel vector is along the  $y$ -axis. The Fermi energy is set at the VBM.

the Néel direction along  $y$ -direction. The alternating magnetic arrangement leads to the opposite spin distribution between  $L_1 - \Gamma$  and  $\Gamma - L_2$ . The asymmetry between  $L_2$  and  $L'_2$  is the consequence of the sixfold symmetry breaking. The twofold rotational symmetry implies three inequivalent pairs of  $k$ -points, where the remaining are  $M_2$ ,  $H_2$ ,  $K_2$ . They are not explicitly shown because all  $M$ ,  $H$  and  $K$   $k$ -points share features analogous to those of  $L$   $k$ -points.

### IN-PLANE COMPONENT OF THE ORBITAL MAGNETIZATION

In this Section, we report the in-plane  $k$ -resolved orbital magnetization  $M_x^{orb}(\mathbf{k})$  and  $M_y^{orb}(\mathbf{k})$  compared with the out-of-plane component  $M_z^{orb}(\mathbf{k})$ . Figure 8(a) shows that  $M_x^{orb}(\mathbf{k})$  and  $M_y^{orb}(\mathbf{k})$  are an order of magnitude smaller than  $M_z^{orb}(\mathbf{k})$ . With respect to Fig. 5 of the main text, it is easier to observe that the orbital magnetization along  $\Gamma - L_1$  is symmetry-inequivalent to that along  $\Gamma - L'_2$ , as expected. Electron-doping near the conduction band minimum does not contribute to orbital magnetization as shown in Fig. 8(b).

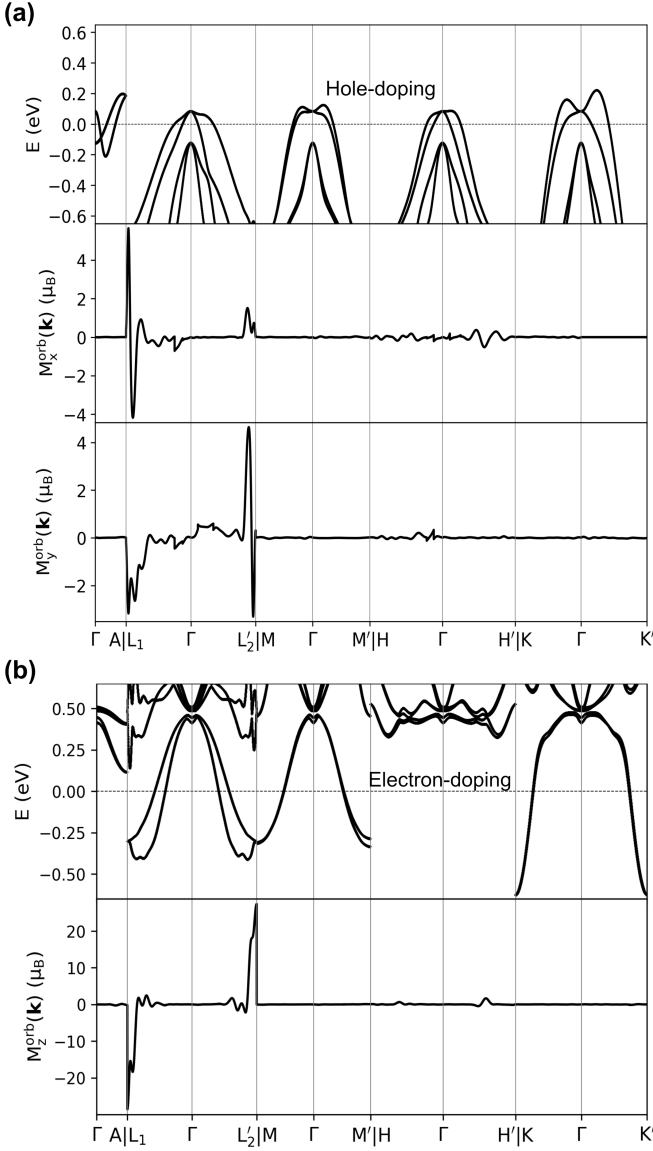


Figure 8. **Calculated k-resolved orbital magnetization**  $M_x^{orb}(\mathbf{k})$ ,  $M_y^{orb}(\mathbf{k})$  and  $M_z^{orb}(\mathbf{k})$ . Orbital magnetization along  $k$ -paths for (a)  $E_F = E_{VBM} - 0.23$  eV (Fermi level in the valence band) and (b)  $E_F = E_{CBM} + 0.55$  eV (Fermi level in the conduction band).  $E_{VBM}$  and  $E_{CBM}$  are the energies of the VBM and CBM, respectively.  $M_z(\mathbf{k})$  is always the dominant term. The peaks of the orbital magnetization originate from energy bands buried deeply in the occupied part of the spectra due to the cumulative aspect of the orbital magnetization.

### ANALYTIC EVALUATION OF THE CANTING ANGLE

The canting angle comes from the competition between the symmetric interaction and magnetocrystalline anisotropy (favoring the collinear phase) and the antisymmetric SOC-driven spin interaction (favoring noncollinearity). In our convention, the first-neighbor antiferromagnetic exchange is  $J > 0$ , while the magnetocrystalline

anisotropy is  $K_2 > 0$ . The first-neighbor antiferromagnetic exchange  $J$  is the inter-sublattice exchange between the two Mn atoms at different  $z$ -coordinates. The most studied antisymmetric SOC-driven spin interaction is the staggered DMI, which is of the first order in the spin-orbit coupling [26] and named  $D$ . In MnTe, the antisymmetric SOC-driven spin interaction is of the second order with respect to the SOC, and we named it  $D_2$ . It can be positive or negative, depending on the conventions used for the unit cell. Since  $D_2$  is a second-order term in the SOC, it is supposed to be smaller than first-order terms like the staggered DMI. Following the literature [24], the total magnetic energy can be expressed as the sum of the Heisenberg part (symmetric interaction), the SOC-driven (antisymmetric interaction) and the magnetocrystalline anisotropy. Since we know the symmetries of the spins of  $Mn_1$  and  $Mn_2$ , we can write them as  $\mathbf{S}^{Mn_1} = (0, S \cos(\theta), S \sin(\theta))$  and  $\mathbf{S}^{Mn_2} = (0, -S \cos(\theta), S \sin(\theta))$  where  $S$  is the module of the spin vector,  $\theta$  is the canting angle and the rotation of the Néel vector is neglected. We consider the case where the Néel vector  $\mathbf{N}$  is parallel to  $y$ . Assuming the Mn spins  $S$  as constant, then the total magnetic energy as a function of the canting angle  $\theta$  reads:

$$E(\theta) = -2JS^2 \cos(2\theta) + D_2 M_z N_y (3N_x^2 - N_y^2) + 2K_2 S^2 \sin^2(\theta) \quad \mathbf{N} \parallel \mathbf{y} \quad (2)$$

Using the formulas for  $\mathbf{S}^{Mn_1}$  and  $\mathbf{S}^{Mn_2}$ , the Néel vector and the magnetization can be written as  $N_x = 0$ ,  $N_y = 2S \cos(\theta)$ , and  $M_z = 2S \sin(\theta)$ . Therefore, the magnetic energy becomes

$$E(\theta) = -2JS^2 \cos(2\theta) - 16D_2 S^4 \sin(\theta) \cos^3(\theta) + 2K_2 S^2 \sin^2(\theta) \quad \mathbf{N} \parallel \mathbf{y} \quad (3)$$

By deriving the previous equation with respect to the canting angle, we obtain

$$\partial_\theta E(\theta) = (4J + 2K_2) S^2 \sin(2\theta) - 8D_2 S^4 (\cos(2\theta) + \cos(4\theta)) \quad (4)$$

The equilibrium canting angle  $\bar{\theta}$  is the minimum of the energy of the system and is the solution of the above derivative equal to zero,  $\partial_\theta E(\theta = \bar{\theta}) = 0$ . For small values of  $\theta$ , we can approximate  $\cos(2\theta) \approx \cos(4\theta)$  from which we arrive

$$\tan(2\bar{\theta}) \approx \frac{8D_2 S^2}{2J + K_2} \quad (5)$$

We observe from the above Eq. (5) that  $J$  and  $K_2$  cooperate to suppress the equilibrium canting angle in MnTe. We can further approximate the previous equation as

$$\bar{\theta} \approx \frac{4D_2 S^2}{2J + K_2} \quad (6)$$

From the intrinsic weak ferromagnetism, the net spin magnetization per unit cell is

$$M_z^{spin} = 2S \sin(\bar{\theta}) \approx 2S\bar{\theta} \approx \frac{8D_2S^3}{2J + K_2} \quad (7)$$

Therefore, in the limit of small  $\bar{\theta}$ , the equation for the equilibrium canting angle in MnTe returns a qualitatively similar result derived for the staggered DMI [24]. To map the results for the staggered DMI in this one for  $D_2$ , we just need to replace the staggered DMI parameter with its higher-order analog  $D_2$ . Since the Néel temperature of MnTe is above room temperature, the value of  $J$  is relatively large, making the canting angle for MnTe quite small. Additionally, the band gap tends to suppress the  $D_2$  value as discussed in the main text.

The total magnetic energy  $E$  of the system is at the first order in  $\bar{\theta}$  and is equal to  $E(\bar{\theta}) = -2JS^2 - 16D_2S^4\bar{\theta} + 2K_2S^2\bar{\theta}^2$  from which we have that the total energy and, therefore, the Néel temperature is dominated by the magnetic coupling  $J$ .

## SUPPRESSION OF THE WEAK FERROMAGNETISM AT HALF FILLING

The spin-orbit operator,  $H_{\text{SOC}} = \lambda \mathbf{L} \cdot \mathbf{S}$ , decomposed using angular momentum ladder operators yields:

$$H_{\text{SOC}} = \lambda \left( L_z S_z + \frac{1}{2}(L_+ S_- + L_- S_+) \right),$$

where  $L_z S_z$  is the spin-conserving and  $\frac{1}{2}(L_+ S_- + L_- S_+)$  is the spin-nonconserving (spin-flip) part. The nonconserving part produces the rotations of the spins and acts as a nondiagonal term between the spins. Let us consider the subsector formed by the orbitals  $xy \uparrow$  and  $yz \downarrow$  on the same Mn site with their respective energy on-site and connected by the non-spin-conserving part of the spin-orbit. This subsector of the Hamiltonian reads:

$$H = \begin{pmatrix} \varepsilon_{xy\uparrow} & \frac{\lambda}{2} \\ \frac{\lambda}{2} & \varepsilon_{yz\downarrow} \end{pmatrix}$$

where  $\lambda$  is the SOC constant, while  $\varepsilon_{xy\uparrow}$  and  $\varepsilon_{yz\downarrow}$  are the respective energies on-site. Assuming  $\varepsilon_{xy\uparrow} < \varepsilon_{yz\downarrow}$ , the eigenvalues  $\varepsilon_+$  and  $\varepsilon_-$  are in the limit of  $\lambda \ll (\varepsilon_{yz\downarrow} - \varepsilon_{xy\uparrow})$ :

$$\varepsilon_+ = \varepsilon_{yz\downarrow} + \frac{\lambda^2}{4(\varepsilon_{yz\downarrow} - \varepsilon_{xy\uparrow})} \quad (8)$$

$$\varepsilon_- = \varepsilon_{xy\uparrow} - \frac{\lambda^2}{4(\varepsilon_{yz\downarrow} - \varepsilon_{xy\uparrow})} \quad (9)$$

where the same term  $\frac{\lambda^2}{\varepsilon_{yz\downarrow} - \varepsilon_{xy\uparrow}}$  is also the first-order correction in the eigenvectors. In the limit of an infinite gap and fully filled valence band, we also have that the term  $\frac{\lambda^2}{\varepsilon_{yz\downarrow} - \varepsilon_{xy\uparrow}}$  goes to zero, therefore, the suppression of the weak ferromagnetism is expected.